International Journal of Nanomedicine

Dovepress
open access to scientific and medical research

Open Access Full Text Article

ORIGINAL RESEARCH

Functionalized Prussian Blue Nanozyme as Dual-Responsive Drug Therapeutic Nanoplatform Against Maxillofacial Infection via Macrophage Polarization

Junlong Da[1], Ying Li[1], Kai Zhang[1], Junyu Ren[1], Jianqun Wang[1], Xinpeng Liu[1], Xiaoyao Liu[2], Jiahui Zhang[1], Lixue Liu[1], Wenxuan Zhang[1], Shujian Zhang[1], Yuyao Guo[1], Bin Zhang[1,3], Han Jin[1]

[1]Heilongjiang Provincial Key Laboratory of Hard Tissue Development and Regeneration, the Second Affiliated Hospital of Harbin Medical University, Harbin, People's Republic of China; [2]Department of Orthodontics, the First Affiliated Hospital of Harbin Medical University, Harbin, People's Republic of China; [3]Heilongjiang Academy of Medical Sciences, Harbin, People's Republic of China

Correspondence: Han Jin; Bin Zhang, Heilongjiang Provincial Key Laboratory of Hard Tissue Development and Regeneration, the Second Affiliated Hospital of Harbin Medical University, Harbin, 150001, People's Republic of China, Tel/Fax +86 0451-86297231, Email jinhan@hrbmu.edu.cn; zhangbin@hrbmu.edu.cn

Purpose: Maxillofacial infection is a common disease in stomatology and is difficult to treat owing to its high potential to spread to vital anatomical structures. Excessive levels of reactive oxygen species (ROS) in infected tissues lead to cellular damage and impede tissue regeneration. However, uncontrollable strategies to remove ROS have limited therapeutic efficacy. Nanoparticle systems for scavenging ROS and remodeling the inflammatory microenvironment offer much promise in the treatment of maxillofacial inflammation.

Methods: Here, a novel microenvironment-stimuli-responsive drug delivery nanoplatform (HMPB@Cur@PDA) based on a polydopamine (PDA)-functionalized hollow mesoporous Prussian blue (HMPB) nanozyme was developed for the delivery of curcumin (Cur) in the treatment of maxillofacial infection. Low pH and excess ROS in the inflammatory microenvironment cause degradation of the outer PDA layer of the nanocomplex, exposing the HMPB nanozyme and loaded Cur, which synergistically act as a ROS scavenger and anti-inflammatory agent, respectively, and induce macrophage polarization from the pro-inflammatory M1 to the anti-inflammatory M2 phenotype.

Results: Experiments in vitro provided strong evidence for the application of novel nanocomplexes in scavenging multiple ROS and inhibiting lipopolysaccharide-induced inflammation. In addition, in vivo results obtained using a mouse maxillofacial infection model demonstrated that HMPB@Cur@PDA had excellent biocompatibility, significantly attenuated the inflammatory response in periodontal tissue, and improved the repair of damaged tissue.

Conclusion: Our results indicate that HMPB@Cur@PDA nanocomposites have great potential for ROS regulation as well as having anti-inflammatory effects, providing new insights for the development of dual-response maxillofacial infection treatments.

Keywords: maxillofacial infection, Prussian blue, nanozyme, polydopamine, reactive oxygen species, macrophage polarization

Introduction

Oral and maxillofacial infections mainly have odontogenic causes, that is, they originate from the tooth or its supporting tissue. Owing to its particular anatomical characteristics, the oral and maxillofacial region is highly susceptible to the spread of infection; thus, an infection that is not treated promptly and effectively may lead to cellulitis and osteomyelitis, and even develop into a life-threatening event in severe cases.[1–3] Currently, antibiotic-assisted anti-inflammatory therapy is frequently used in clinical practice. Although admirable results have been achieved, there is still little escape from the problem of resistance to widely used antibiotics.[4,5] Therefore, new therapies with anti-inflammatory and pro-repair capabilities are necessary for the development of a rational strategy for the treatment of oral infections.

Received: 12 August 2022
Accepted: 18 November 2022
Published: 30 November 2022

During the pathological process of maxillofacial infection, tissue destruction occurs when the balance between pathogenic bacteria and the immune response is destabilized. Briefly, the invading pathogen and its harmful metabolites trigger an innate immune response, in which immune cells (mainly macrophages and neutrophils) are recruited and activated in the affected regions. Pro-inflammatory cytokines and reactive oxygen species (ROS) such as hydrogen peroxide (H_2O_2), superoxide ($O_2•^-$), hydroxyl radicals (•OH), and singlet oxygen ($^1O_2$) are released.[6–8] The production of ROS by immune cells disrupts the balance of oxidative and antioxidant defense systems (eg, catalase (CAT), superoxide dismutase (SOD), and glutathione peroxidase), leading to oxidative stress, which is considered to be an integral part of the pathogenesis of inflammation.[9] Excess ROS directly cause oxidative damage to proteins, lipids, DNA, and other biomolecules; this is a central link in the progression of inflammatory disease.[10] In addition, ROS promote inflammation and apoptosis by activating the NF-κB and JNK signaling pathways, respectively.[11,12] Recent studies suggest that ROS may have a crucial role in regulating macrophage phenotype.[13,14] Macrophage populations are generally divided into classically activated M1 macrophages, which remove pathogens by secreting pro-inflammatory cytokines (eg, TNF-α, IL-1β), and alternatively activated M2 macrophages, which promote tissue repair and wound healing by generating anti-inflammatory cytokines (eg, TGF-β and IL-10). These two phenotypes have different roles in the immune system.[15,16] M2 activation is accompanied by reduced ROS production compared with M1 macrophages.[17] Therefore, scavenging ROS, remodeling the inflammatory microenvironment with M2 phenotypic polarization, and reducing inflammation may represent a promising strategy for treatment of maxillofacial inflammation.

With advances in nanotechnology, antioxidant nanocomplexes based on natural enzymes and nanozymes have achieved impressive results in scavenging ROS. Nanozymes have the unique bioactive ability to mimic natural enzymes (superoxide oxidase, CAT, etc.). They also have the advantages of low cost, high catalytic activity, easy modification, and high tolerance to the external environment compared with natural enzymes.[18,19] As a result, nanozymes are the subject of increasing attention in the field of life sciences. Cerium oxide nanozymes are widely used as antioxidants and free radical scavengers in treatment strategies for a variety of diseases, including spinal cord injury,[20] liver injury,[21] and periodontitis.[22] However, recent studies have reported that cerium oxide nanoparticles (NPs) remain in the body for 1 month after intravenous administration.[23,24] Other nanozymes, including manganese oxide NPs, platinum NPs, and carbon nanotubes, have also been used in antioxidant therapy; however, their potential side effects and complicated preparation methods may limit their clinical applications. Therefore, the long-term biosafety of nanomaterials requires detailed discussion. Prussian blue (PB) has been approved by the Food and Drug Administration as an antidote for the treatment of exposure to radioactive elements thallium and cesium. PB has CAT, SOD, and peroxidase (POD) mimetic enzymatic activity and extremely high biosafety.[25,26] A series of recent studies suggest that PB nanozymes could be used to scavenge ROS and manage inflammation to prevent anthracycline-induced liver injury,[27] improve acute pancreatitis,[28] and promote healing of full-thickness skin wounds.[25] Based on these findings, it is reasonable to expect PB to be a safe and effective nanoformulation for the treatment of maxillofacial inflammation.

Local administration of drugs has been extensively used in the treatment of maxillofacial inflammation, as it has the advantages of directly targeting the lesion and avoiding systemic toxicity. However, this strategy may raise concerns, for instance, about uncontrollable local drug release, which can result in insufficient or excessive drug concentrations.[29] Recently, stimulus-responsive drug delivery systems based on the properties of the oral and maxillofacial inflammatory microenvironment have demonstrated great promise for applications in oral tissue engineering.[30–32] Maxillofacial inflammation may contribute to a relatively acidic microenvironment (pH 5.0–7.0) and high levels of ROS and extracellular matrix metalloproteinases (MMPs).[33] Therefore, researchers developed a pH-, ROS-, and MMP8-responsive platform for the treatment of maxillofacial inflammatory, which could release cargoes in response to the corresponding environmental stimuli to improve the therapeutic effects of oral and maxillofacial inflammatory treatments. Inspired by this research, we developed a nanodrug delivery platform with dual pH and ROS response using polydopamine (PDA), a mussel-inspired natural polymer with excellent biocompatibility,[34] as a coating. Low pH and excess ROS change the interlayer structure of PDA to release the loaded drug.[35–37] Thus, PDA-coated NPs with dual response properties may represent a novel drug delivery strategy for the treatment of oral and maxillofacial inflammation.

Curcumin (Cur), a candidate drug for treatment of periodontitis, is an active natural polyphenolic molecule extracted from root of turmeric.[38,39] It exhibits a variety of pharmacological properties including anti-inflammatory, anti-cancer, and antioxidant activities. However, the low water solubility and poor oral bioavailability of Cur limit its clinical applications.[40,41] Nanoformulation is a potential approach to improve the physiologically mediated stability and bioavailability of Cur to enhance

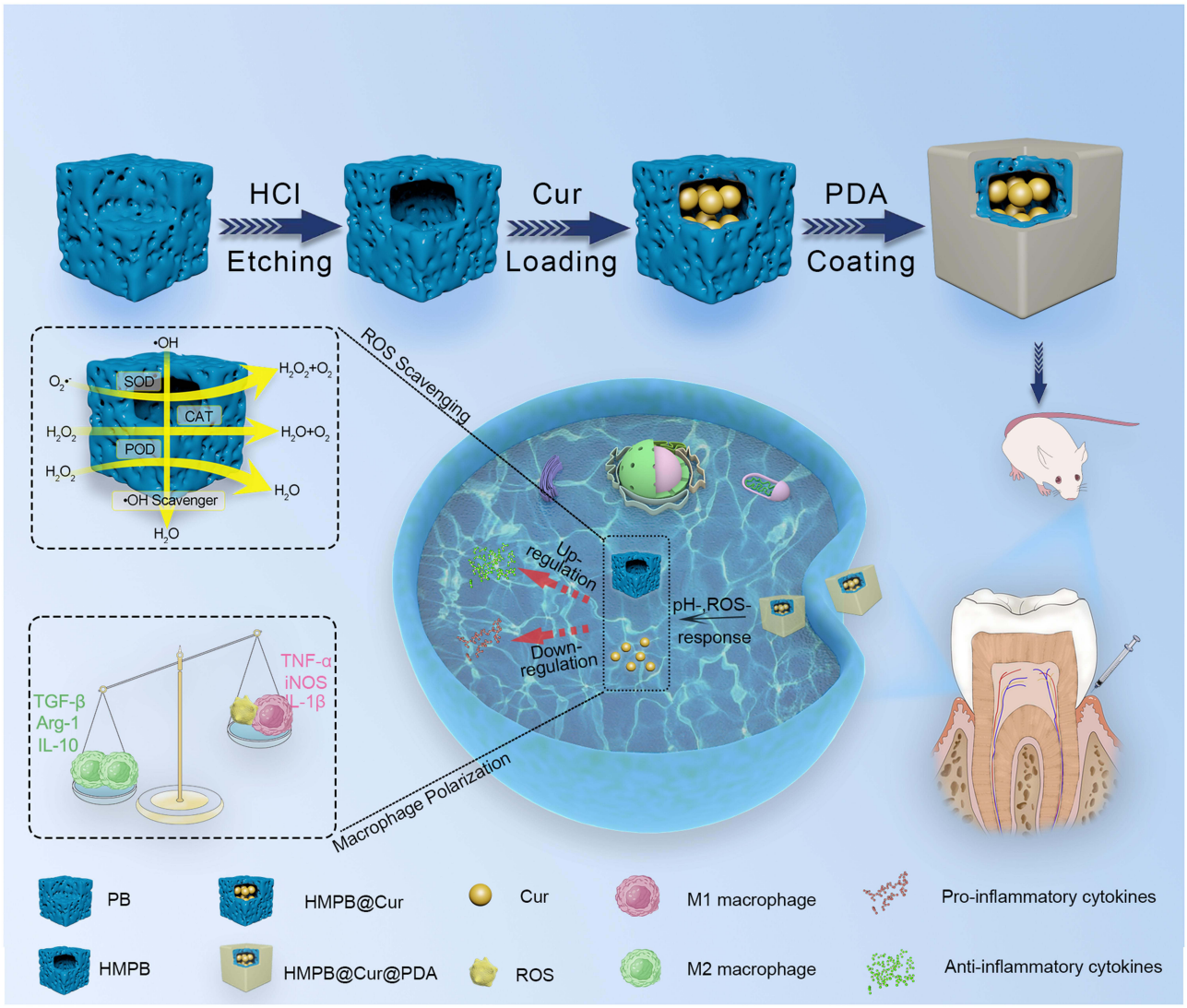

Scheme 1 Schematic illustrations of HMPB@Cur@PDA synthesis and the potential therapeutic mechanisms of the ROS- and pH-responsive drug release system in oral and maxillofacial inflammatory diseases involving attenuation of ROS and regulation of inflammatory response.

its therapeutic benefits. In the present study, dual-responsive NPs with multiple therapeutic effects were synthesized according to the route shown in Scheme 1. In these particles, PDA acts as a gatekeeper to expose hollow mesoporous PB (HMPB) and release HMPB-loaded Cur under the stimulation of the inflammatory microenvironment. HMPB and Cur acting synergistically scavenged higher levels of ROS, induced the reversal of macrophage polarization from M1 to M2, prevented the progression of inflammatory tissue destruction, and promoted the regeneration of tissue. These results indicate the potential of our HMPB@Cur@PDA particles as a new approach to the treatment of oral and maxillofacial inflammation and even other inflammatory diseases.

Materials and Methods

Materials

$K_3[Fe(CN)_6]$, Dopamine hydrochloride, lipopolysaccharide (LPS), 2',7'-dichlorofluorescein diacetate (DCFH-DA) were purchased from Aladdin Reagent Co., Ltd (Shanghai, China). Poly(vinylpyrrolidone) (PVP, K30) and Curcumin (Cur) were commercially obtained from Solarbio Technology Co., Ltd. (Beijing, China). RAW264.7 was supplied by Jilin University and authenticated using short tandem repeat (STR) profiling analysis. Dulbecco's modified Eagle's medium (DMEM), penicillin/streptomycin and fetal bovine serum (FBS) were acquired from Gibco (Grand Island, NY, USA).

Preparation of HMPB

HMPB was synthesized according to a method described in the previous literature.[42] Briefly, PVP (9.0 g), $K_3[Fe(CN)_6]$ (396 mg), and HCl (0.01 M, 120 mL) were mixed using a magnetic stirrer for 30 min until the solution was clarified. The container was put into an electric oven at 80°C for 24 h. Then, the mesoporous PB NPs were collected by centrifugation and washed in distilled water and ethanol several times. In a typical procedure, PVP (200 mg) and PB (40 mg) were added to HCl solution (1.0 M, 40 mL) under magnetic stirring. After 3 h of stirring, the solution was transferred into a stainless autoclave and heated at 140°C for 4 h. HMPB was obtained by centrifugation at 12,000 rpm for 10 min and washed with distilled water three times.

Preparation of HMPB@Cur@PDA

To obtain HMPB@Cur particles, Cur (10 mg) and HMPB (5 mg) were dissolved in ethanol and stirred for 24 h in the dark at room temperature. The resulting Cur-loaded HMPB was collected by centrifugation and freeze drying. The amount of unbound Cur was calculated by ultraviolet–visible light (UV–vis)–near-infrared spectroscopy with an absorption intensity of 425 nm.

PDA-coated HMPB@Cur was prepared via a classical in situ polymerization process. In brief, 5 mg of HMPB@Cur was added to 20 mL of Tris-HCl solution (10 mM, pH 8.5) containing 10 mg of dopamine hydrochloride. The mixed solution was stirred at 25°C for 4 h. The precipitate (HMPB@Cur@PDA) was collected by centrifugation and dissolved in distilled water for further use. HMPB@PDA was prepared by the same synthesis strategy without addition of Cur.

Characterization

Transmission electron microscope (TEM, Hitachi HT7800, Japan) were used to observe the morphology and structure of samples. Fourier transform infrared (FTIR) spectroscopy was investigated by an FTIR spectrometer (Thermo Scientific, USA). The solution absorbance of NPs was measured by an UV−visible spectrometer (Shimadzu UV-2600, Japan). BI-90Plus (Brookhaven Instruments, US) was employed to analyze ζ-potential of NPs. X-ray diffraction (XRD, Shimadzu XD-D1) was applied to measure the crystal structure. The X-ray photoelectron spectroscopy (XPS) analysis was examined with an XPS spectrometer (Thermo Scientific 250Xi, USA).

Stimulus-Responsive Drug Release

To assess the pH- and ROS-triggered drug release process, 1 mL of HMPB@Cur@PDA (1 mg/mL) was dispersed in dialysis bags (molecular weight cut-off, 3.5 kDa) and immersed in 15 mL of buffer with pH values of 7.4, 6.0, and 5.0, respectively. For ROS-stimulated drug release, H_2O_2 at a final concentration of 20 mM was added to the buffer at pH = 7.4, followed by shaking at 200 rpm at room temperature. At specific time intervals, 0.5 mL of culture supernatant was collected and replaced with an equal amount of buffer to keep the volume stable. The total released Cur was measured using a multifunctional microplate reader, and a release curve was constructed.

SOD-Like Activity

To measure the SOD activity of NPs, HMPB@Cur@PDA was incubated with 10 mM H_2O_2 at 37°C for 12 h and collected by centrifugation. The SOD-like activity of NPs at different concentrations was analyzed using a SOD assay kit (Solarbio, China) based on the production of formazan, which is generated by superoxide anions reacting with nitro blue tetrazolium (NBT). Formazan (which has an absorption peak at 560 nm) was quantified using a multifunctional microplate reader.

H_2O_2 Degradation Activity

The H_2O_2 degradation activity of NPs was assessed using a H_2O_2 assay kit (Solarbio, China). HMPB@Cur@PDA at different concentrations was added to 10 mM H_2O_2 solution and incubated with shaking at room temperature. After 2 h, the mixture was centrifuged at 11,000 rpm for 10 min and the supernatant was collected. The remaining H_2O_2 in the supernatant was analyzed according to the protocol of the reagent manufacturer.

POD-Like Activity

First, NPs were incubated with 10 mM H_2O_2 for 12 h to simulate the ROS environment. Then, the absorbance values at 650 nm of the solution containing 2 mL Hac-NaAc buffer (pH 4.0), 0.2 mL of different concentrations of NPs, 0.16 mL 3, 3', 5, 5'-tetramethylbenzidine (TMB) (10 mg/mL), and 0.32 mL H_2O_2 (30%) were recorded using a spectrophotometer.

$O_2•^-$ Scavenging Capacity

Mixtures containing methionine (25 mM), riboflavin (40 μM), NBT (150 μM), and HMPB@Cur@PDA NPs were irradiated with UV for 20 min. After illumination, the $O_2•^-$ scavenging efficiency of HMPB@Cur@PDA was assessed by measuring the absorbances of the mixtures. The inhibition rate was calculated according to the following formula: inhibition ratio = [(Ax-An) /(Ap-An)] x 100%, where Ax is the absorbance of the treated samples with NPs; An is the absorbance of the samples containing methionine, riboflavin, and NBT; and Ap is the absorbance of the samples containing methionine, riboflavin, and NBT after UV irradiation.

•OH Scavenging Capacity

The •OH scavenging of HMPB@Cur@PDA was determined by UV-vis spectrophotometer, based on the salicylic acid reacts with •OH to generate 2,3-dihydroxybenzoic acid with an absorption peak at 510nm. In short, •OH are generated by Fenton reaction: H_2O_2 (8.8 mM) and $FeSO_4$ (9 mM) were added into deionized water and mixed for 5 min. And then, HMPB@Cur@PDA of different concentrations were added into the solution and incubated at 37°C for another 15 min. Finally, salicylic acid (9 mM) was added to detect the remaining •OH by generating a purple solution, which is measured by UV spectrophotometer.

•DPPH Scavenging Capacity

The 0.1mM DPPH working solution was formulated by mixing with ethanol. DPPH (0.7 mL) was mixed with different concentrations of HMPB@Cur@PDA (0.1 mL), and after incubation for 30 min in the dark at room temperature, the absorbance at 517 nm was measured by UV spectrophotometer. The mixture of deionized water with DPPH served as the blank control.

Hemolysis Assay

Fresh whole blood was taken through the inner canthus vein of mice, and red blood cells (RBC) were isolated from serum by centrifugation. After washing three times with phosphate-buffered saline (PBS), RBC were diluted to an approximate 4% (v/v) suspension in PBS. HMPB@Cur@PDA NPs were added to the erythrocyte suspension at different concentrations (0.05, 0.1, 0.2, 0.5, and 1 mg/mL). Diluted RBC were mixed with PBS and 0.1% (v/v) Triton X-100 as negative and positive controls, respectively. After 3 h incubation at 37°C, the mixtures were centrifuged and the supernatants were collected. A multifunctional microplate reader was used to detect the absorbance of supernatant at 540 nm (n = 3). The hemolysis rate as calculated by the following formula: hemolysis (%) = (A-A0)/(A1- A0) × 100%, where A, A0, and A1 indicate the absorbances of the sample, negative control, and positive control, respectively.

Cell Cultures

Human gingival fibroblasts (HGFs) were isolated from the gingival tissue of orthodontic patients aged 15–20 years, which was approved by the Medical Ethics Committee of the Second Affiliated Hospital of Harbin Medical University (Document No. KY2022-154). HGFs were identified by Immunocytochemistry staining for cytokeratin and keratin. HGFs and RAW264.7 were both maintained in DMEM, which were supplemented with 10% FBS and 1% penicillin/streptomycin at 37°C in 5% CO_2 atmosphere. The HGFs applied in subsequent experiments were in the range of passages 4–6.

Cytotoxicity Studies

The cell viability of HGFs and RAW264.7 cells was measured by CCK-8 assay. Cells were seeded into 96-well plates at a density of 6×10^3 cells per well and incubated for 12 h. HMPB@Cur@PDA at different concentrations was added to the medium. After incubation for 24 h, the cell culture medium was replaced with medium containing 10% CCK-8 for another 2 h. The absorbance was examined at 450 nm with a Bio-Rad microplate reader.

For cellular viability observation, HGFs were seeded in a 96-well plate and treated with HMPB@Cur@PDA (10, 20, 50, 80 and 100 μg/mL) for 24 h. Then, the cells were washed with PBS and stained with Calcein Acetoxymethyl Ester (AM) and Propidium Iodide (PI). Live and dead staining was examined using a fluorescence microscope system.

Intracellular ROS Scavenging

DCFH-DA is widely used as a fluorescent probe to monitor levels of intracellular ROS. HGFs and RAW264.7 cells were plated at a density of 5×10^4 cells per well in 12-well plates. The cells were exposed to lipopolysaccharide (LPS; 1 μg/mL) and NPs at different concentrations for 12 h. The cell medium was replaced with fetal-bovine-serum-free medium with 10 μM DCFH-DA at 37°C followed by incubation for 30 min in the dark. After cells had been washed with PBS three times, the intracellular ROS levels were observed by fluorescence microscopy. Cells without any treatment were used as the control group.

Immunofluorescence Staining

HGFs were treated with different NPs and prepared as previously described. In brief, all groups were fixed with 4% paraformaldehyde and permeabilized with 0.5% Triton X-100 in PBS for 30 min at room temperature. Bovine serum albumin (3%) in PBS was used to block nonspecific binding sites. Rabbit anti-IL-1β was incubated with samples as a primary antibody overnight at 4°C. Alexa Fluor 488-conjugated goat anti-rabbit IgG (Sangon Biotech, Shanghai, China) was used as a secondary antibody. Nuclei were counterstained using DAPI for 5 min. After cells had been rinsed in PBS, they were visualized using a fluorescence microscope.

Quantitative Real-Time Polymerase Chain Reaction (RT-qPCR) and Enzyme-Linked Immunosorbent Assay (ELISA)

HGFs and RAW264.7 cells were plated in six-well plates at a density of 2×10^5 and stimulated by LPS (1 μg/mL) with or without NPs. After 24 h incubation, total RNA of cells was isolated and purified using TRIzol according to the manufacturer's instructions. Then, 1 μg of extracted total RNA was reverse transcribed to cDNA using a PrimeScript RT kit on a Bio-Rad thermal cycler. RT-qPCR was used to investigate the mRNA expression of inflammatory cytokines using SYBR Premix Ex Taq II kits. The primer sequences for RT-qPCR are listed in Table S1. β-actin was used as an internal control for normalization. The relative expression of mRNA was calculated by the $2^{-\Delta\Delta Ct}$ method.

To detect inflammatory cytokines and chemokines, the cell culture medium was carefully collected and centrifuged. The concentrations of proinflammatory cytokines including IL-1β and TNF-α were determined using a mouse ELISA kit (Ruixinbio, Quanzhou, China) according to the manufacturer's instructions.

Animals

ICR mice (25±5g) for use in this research were approved by the Institutional Animal Care and Use Committee of Harbin Medical University (Approved protocol No.SYDW2022-079). All animal procedures were performed in strict accordance with the Guidelines for the Care and Use of Laboratory Animals.

To construct experimental oral and maxillofacial inflammation in ICR mice, LPS (1 mg/mL, 20 μL) diluted with PBS was subgingivally injected at the site of the mandibular incisor for 3 days after anesthesia. Different types of NPs were injected at 20 μg/site for each group. After 4 days of treatment, digital photos were taken to record the inflammatory state of the gingiva.

ROS probe DCFH-DA (600 μM, 20 μL) was locally injected in situ to evaluate ROS level in vivo by an animal imaging system (excitation filter: 500 nm, emission filter: 600 nm, Bruker). Mice were then sacrificed, and the mandibles and main organs were fixed with 4% paraformaldehyde for 24 h. The mandibles were decalcified in 15% EDTA solution at 4°C for 2 weeks, and all samples were embedded in paraffin and sectioned at a thickness of 5 μm for hematoxylin and eosin (H&E) or immunohistochemistry (IHC) analyses.

Statistical Analysis

All results were expressed as means ± standard deviations. All statistical significance was conducted by one-way analysis of variance (ANOVA) for multiple comparisons (* $P < 0.05$, ** $P < 0.01$, *** $P < 0.001$, **** $P < 0.0001$).

Results and Discussion

Fabrication and Characterization of HMPB@Cur@PDA

The protocol for the synthesis of HMPB@Cur@PDA nanocomposites is shown in Scheme 1. The morphology and structure of HMPB, HMPB@PDA, and HMPB@Cur@PDA were measured by transmission electron microscopy (TEM). Typical TEM images revealed that the obtained NPs had a cubic shape with average diameter of 139 nm for HMPB, 187 nm for HMPB@PDA, and 188 nm for HMPB@Cur@PDA (Figures 1A–C and S1A–C). All NPs exhibited hollow nanostructures. After coating, the PDA layer was homogeneously generated on the surface of HMPB. No significant differences in morphology or structure were observed after the encapsulation of Cur in HMPB@PDA.

The UV–vis absorption spectra are shown in Figure 1D. HMPB exhibited a typical absorption spectrum at 740 nm with broad absorption peaks from 600 nm to 900 nm. After PDA coating, the absorbance peak of HMPB@PDA slightly blue-shifted to 710 nm. For HMPB@Cur@PDA, a new absorption peak appeared at 445 nm due to Cur loading. Fourier transform infrared (FTIR) spectra of the obtained NPs were obtained to validate the chemical groups (Figure 1E).

HMPB showed characteristic peaks at 2070 cm^{-1}, which could be attributed to the stretching vibrations of the C≡N group in Fe^{2+}–Fe^{3+}. A few additional bands originating from Cur appeared in the HMPB@Cur spectrum at approximately 1628, 1601, 1285, and 1028 cm^{-1}; these were assigned to the C=O vibration overlapping with C=C bonds, stretching vibration of C=C aromatic rings, C-O in the aromatic rings, and C-O-C stretching vibration modes, respectively. After coating with PDA, HMPB@Cur@PDA showed specific absorption peaks at 1512 and 1285 cm^{-1}, which were attributed to C=C and C-O in

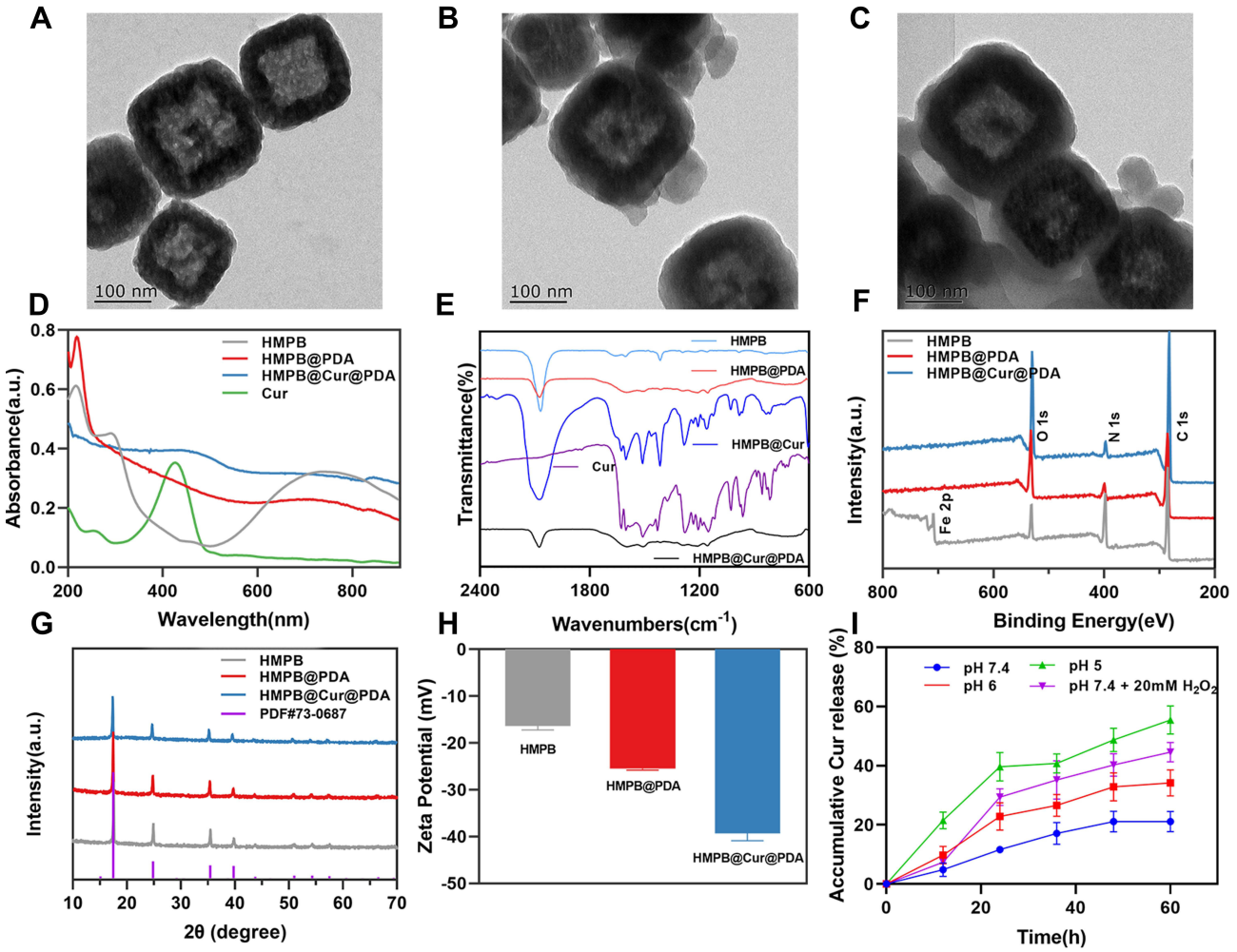

Figure 1 Characterization of NPs: (**A–C**) TEM images of HMPB, HMPB@PDA, and HMPB@Cur@PDA. Scale bar: 100 nm. (**D–H**) UV–vis spectrum, FTIR spectrum, XPS, XRD, and zeta potential of obtained NPs. (**I**) pH-responsive and ROS-responsive Cur release from HMPB@Cur@PDA.

aromatic rings. X-ray photoelectron spectroscopy (XPS, Figure 1F) was performed to investigate the surface chemical compositions of NPs. HMPB showed a binding energy peak at 708.2 originating from Fe 2p; this obvious Fe 2p peak disappeared in the spectra for HMPB@PDA and HMPB@Cur@PDA because of the presence of the PDA layer.

X-ray diffraction (XRD) analysis was used to characterize the crystalline structure of HMPB NPs and revealed diffraction peaks at 2θ angles of 17.5°, 24.8°, 35.4°, and 39.8°; these could be assigned to the distinct diffraction planes of (200), (220), (400), and (420) and were maintained after Cur loading and PDA coating (Figure 1G). Zeta potentials were also measured; the results are displayed in Figure 1H. The zeta potential of HMPB@PDA decreased to −25 mV owing to the negative charges of the PDA layer, whereas the presence of Cur caused a decrease to −39 mV, which was attributed to the phenolic hydroxyl groups of Cur.[43] Overall, these results indicate the successful preparation of HMPB@Cur@PDA nanocomposites.

Dual-Responsive Nanocomposites

The microenvironment at the site of inflammation is mildly acidic, and the level of ROS that causes oxidative stress is higher than that found in the normal physiological state. Therefore, acid- and ROS-sensitive nanoformulations can facilitate the targeted delivery of anti-inflammatory drugs. Dual-response drug release experiments were performed by studying the Cur release profiles of PDA-coated HMPB at different times. Figure 1I shows the pH- and ROS-dependent kinetics of Cur release. Under physiological conditions of pH 7.4, the cumulative release rate of Cur was as low as 11.6% at 24 h and increased to 21.1% at 60 h. By contrast, drug release was accelerated in a slightly acidic environment (pH 6 and 5), with cumulative release rates of Cur of 22.8% and 29.4% at 24 h, respectively, increasing to 34.1% and 44.5% at 60 h. After culture for 60 h in the presence of 20 mM H_2O_2, the cumulative release rate of Cur reached 55.1%, 2.6 times higher than that in the absence of H_2O_2. This triggering of drug release by low pH and ROS could be attributed to exfoliation of the PDA layer from the HMPB surface. Therefore, the dual pH/ROS-responsive HMPB@Cur@PDA nanocomposite may facilitate the cumulative release of Cur at an inflammation site to enhance the therapeutic effect.

Multienzyme-Like Activity and Free Radical Scavenging Activities

A common type of ROS, $O_2\bullet^-$, can be converted to O_2 and H_2O_2 by natural SOD.[44] In order to explore the SOD-like catalytic activity of HMPB@Cur@PDA, different concentrations of NPs were quantified using a SOD Assay Kit based on the xanthine and xanthine oxidase reaction (XO/XOD) system. The results revealed that the SOD-mimetic activity of HMPB@Cur@PDA was concentration-dependent (Figure 2A). The scavenging by NPs of $O_2\bullet^-$ reached 63.8% at an NPs concentration of 200 μg/mL. H_2O_2, another type of destructive ROS, has a longer half-life than $O_2\bullet^-$ and thus can cause more sustained damage to organisms.[45] H_2O_2 can be decomposed into non-toxic O_2 and water via CAT, one of the main antioxidant enzymes.[46] Instead of directly measuring the CAT-like enzyme activity of HMPB@Cur@PDA, we detected its total H_2O_2 scavenging capacity using a H_2O_2 content detection kit.[25] The results showed that with increasing NPs concentration, the amount of remaining H_2O_2 in the reaction system decreased gradually (Figure 2B). At the same time, a large number of bubbles could be clearly seen on the centrifugal pipe wall, which were identified as oxygen.[26] Therefore, we concluded that the NPs showed CAT-like H_2O_2 degradation ability. Furthermore, with the assistance of H_2O_2, a POD-like activity assay, which assesses key enzymes involved in antioxidant defense systems, was carried out using TMB as the POD chromogenic substrate. As shown in Figure 2C, the variation of the absorbance of the control at 650 nm was almost negligible within 10 min. However, the oxidized TMB displayed higher absorbance at the same time point after the addition of different concentrations of HMPB@Cur@PDA, indicating strong POD-like activity of the prepared NPs.

We selected representative free radicals to determine the scavenging rates of free radicals by the NPs. We measured the $O_2\bullet^-$ scavenging activity of HMPB@Cur@PDA by determining the inhibition ratio of photo-reduction of NBT. Riboflavin, methionine, NBT, and UV radiation were also employed. The absorbance around 560 nm was significantly decreased by HMPB@Cur@PDA at increasing concentrations, indicating that HMPB@Cur@PDA possesses excellent scavenging capacity towards $O_2\bullet^-$ (Figure 2D). •OH is among the most destructive and highly reactive ROS and plays a key part in the induction of oxidative damage. The results shown in Figure 2E provide direct evidence for the radical scavenging activity of the NPs. The •OH scavenging efficiency was nearly 60% when the NPs concentration was 200 μg/mL. DPPH, which is a stable free radical, has been widely used to evaluate antioxidant activity. Similar to •OH, DPPH radicals were significantly inhibited by NPs at increasing

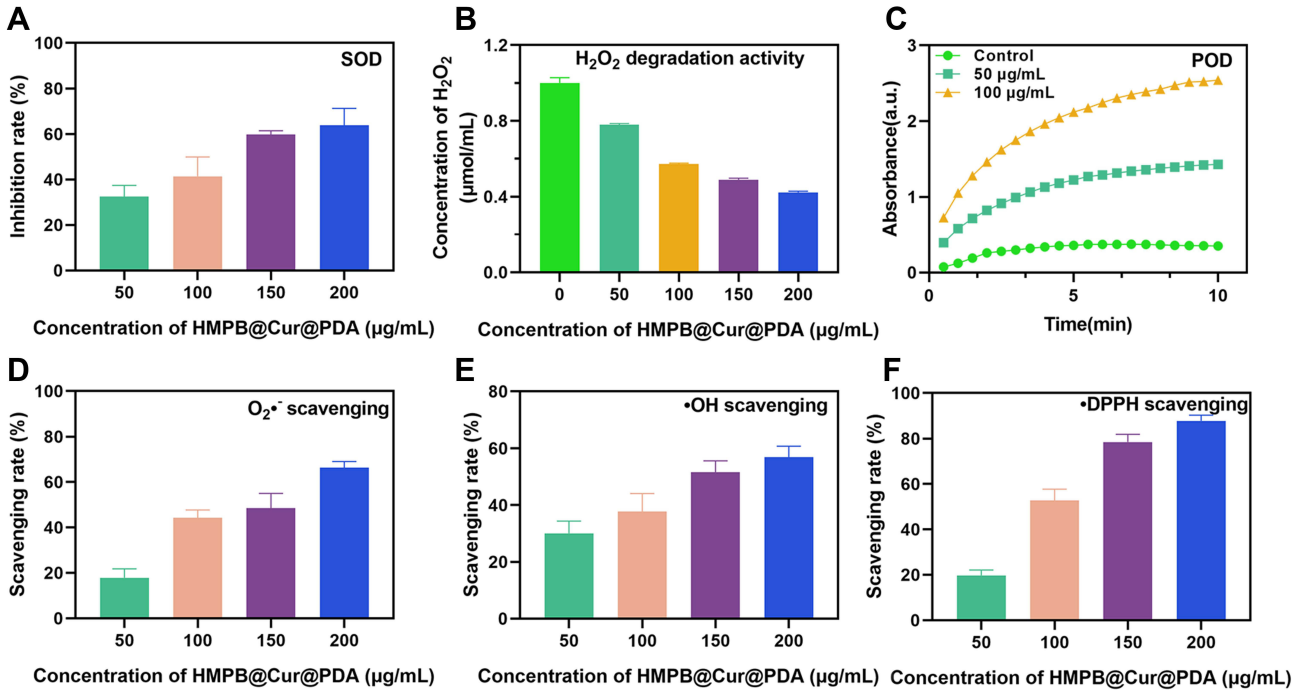

Figure 2 Multienzyme-like activity and free radical scavenging activities of HMPB@Cur@PDA NPs. (**A**) SOD-like activity of HMPB@Cur@PDA. (**B**) Concentration-dependent H_2O_2 degradation by HMPB@Cur@PDA nanozyme through CAT-mimetic activity. (**C**) POD-like activity of HMPB@Cur@PDA. (**D-F**) $O_2^{\bullet-}$, •OH, and •DPPH scavenging ability of HMPB@Cur@PDA at different concentrations. Data are shown as mean ± SD.

concentrations. When the concentration reached 200 μg/mL, NPs exhibited excellent intrinsic DPPH scavenging with an efficiency of almost 90% (Figure 2F).

In summary, these results demonstrate that HMPB@Cur@PDA can effectively convert harmful ROS into harmless molecules in a dose-dependent manner. This implies that the NPs have potential applications in the treatment of oxidative-stress-related oral and maxillofacial inflammatory disease.

In vitro Cytotoxicity

The biosafety of nanocomplexes is the primary consideration in clinical applications. The hemocompatibility of the HMPB@Cur@PDA nanocomplexes with mouse erythrocytes was evaluated, using TritonX-100 as a positive control. As shown in Figure 3A, the hemolysis of erythrocytes by the NPs was negligible even at a high concentration of 1000 μg/mL. Cytotoxicity assays were also performed using CCK-8. As shown in Figure 3B, the RAW264.7 cellular activity at a concentration of 200 μg/mL of HMPB was 54.4% of the control group. HMPB@PDA and HMPB@Cur@PDA barely inhibited RAW264.7 macrophages in the experimental concentration range. HGFs were also used to evaluate the cytotoxicity of NPs. Figure S2 shows the results of the extraction and identification of HGFs. After 6 days of tissue culture, cells were visible from the tissue (Figure S2A). IHC results showed negative immunoreactivity for cytokeratin 8 and positive immunoreactivity for vimentin (Figure S2B and C), suggesting that the harvested cells were HGFs. When stained with phalloidin, the HGFs showed a typical spindle shape under fluorescence microscopy (Figure S2D–F), consistent with the results of previous studies.[47,48] Subsequently, the cytotoxicity of different NPs to the HGFs was assessed by CCK-8 and live/dead staining assays. The results of the CCK-8 assay (Figure 3C) showed that at concentrations below 100 μg/mL of HMPB@Cur@PDA, cell survival was not statistically significantly different from that of the control group. When the concentration reached 100 μg/mL, the NPs exhibited significant cytotoxicity (93% cell viability). Similar cytotoxicity appeared after 5 days of co-culture with RAW264.7 and HGFs using different concentrations of NPs. These results suggest that HMPB@Cur@PDA has negligible cytotoxicity to RAW264.7 and HGFs (Figure S3A and B). Furthermore, fluorescence microscope was used to observe green Calcein-AM-stained live cells and red Propidium-Iodide-stained dead cells. In the fluorescence images (Figure 3D), almost no dead cells (with red

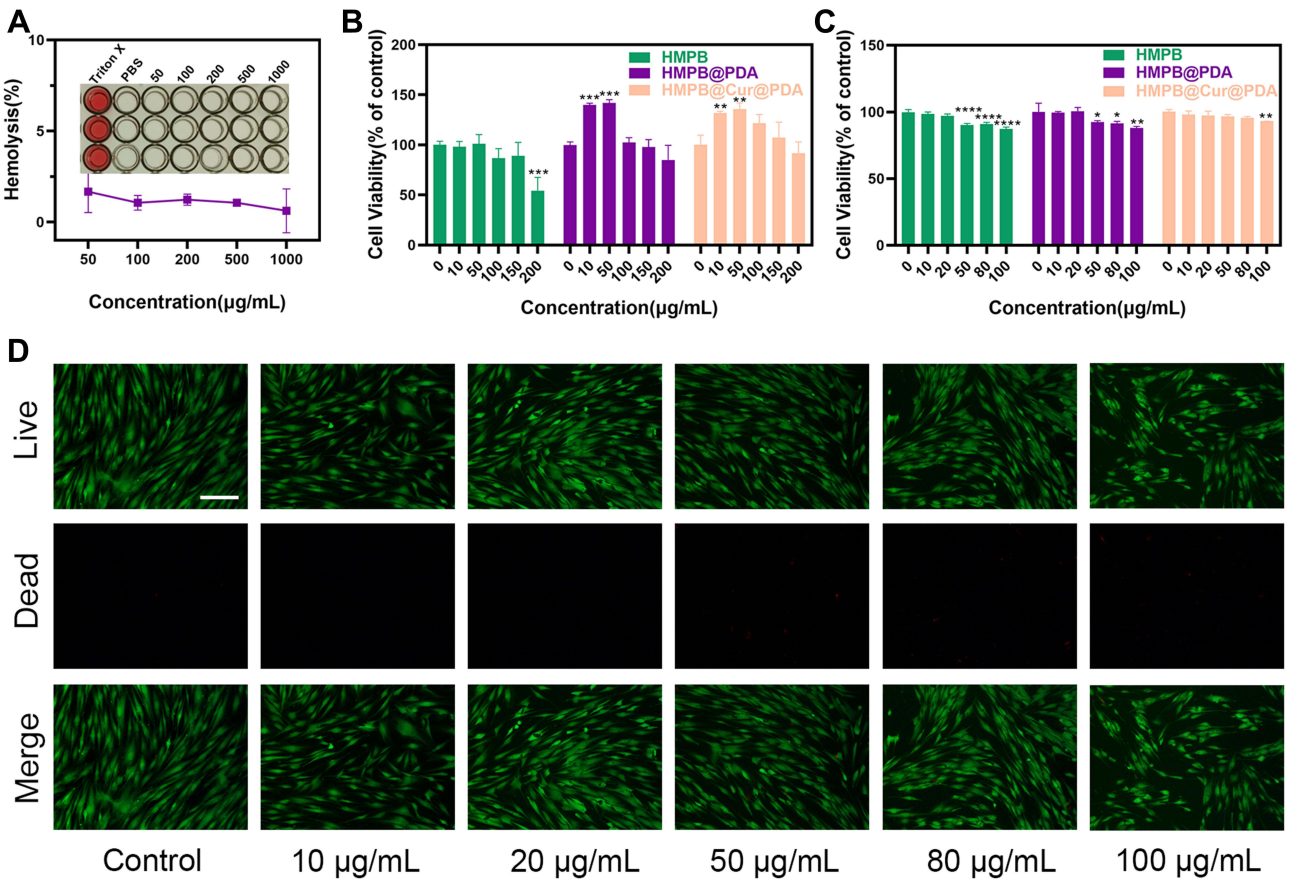

Figure 3 Biosafety analysis in vivo of different concentrations of NPs. (**A**) Hemolysis after treatment of cells with HMPB@Cur@PDA NPs. Viability of RAW264.7 cells (**B**) and HGFs (**C**) incubated with different concentrations of various NPs. (**D**) Live/dead-stained fluorescence images of HGFs incubated with HMPB@Cur@PDA at different concentrations (Scale bar: 50 μm). * $P < 0.05$, ** $P < 0.01$, *** $P < 0.001$, **** $P < 0.0001$.

fluorescence) were observed. These results indicate that HMPB@Cur@PDA has outstanding biocompatibility and is suitable for applications in the clinical treatment of oral and maxillofacial inflammatory disease.

Antioxidative Stress and Anti-Inflammatory Properties in vitro

The presence of large amounts of ROS in inflammatory tissue accelerates tissue damage. To evaluate the effects of HMPB@Cur@PDA on intracellular ROS contents, LPS was used as a ROS inducer to stimulate RAW264.7 cells and HGFs to produce excess ROS. ROS scavenging ability was detected using a DCFH-DA fluorescent probe. As shown in Figure 4A and B, after LPS treatment, the fluorescent probe reacted with ROS to generate DCF with a strong fluorescent signal. However, obvious fluorescence quenching was observed in the HMPB-, HMPB@PDA- and Cur-treated cell groups, indicating that these NPs and Cur have some ROS scavenging activity. In particular, negligible fluorescence was detected in the HMPB@Cur@PDA group, similar to the negative control group without the presence of LPS. These results suggest that HMPB@Cur@PDA has significant intracellular ROS scavenging properties and is protective against cellular oxidative stress damage.

Macrophages have two main phenotypes, M1 and M2. In inflammation, M1 macrophages are predominant and promote inflammatory progression, induce osteoclast formation, and lead to bone resorption by secreting multiple pro-inflammatory cytokines including TNF-α, IL-1β, and iNOS.[49,50] By contrast, M2 macrophages perform long-term functions of inflammation suppression, tissue regeneration, and wound healing by producing anti-inflammatory factors.[51,52] Therefore, modulating endogenous cellular immunity by reversing M1 macrophages to the M2 phenotype is an effective therapeutic approach to eliminate inflammation and repair damaged tissue. Macrophages are highly plastic and can be polarized into different phenotypes under the regulation of the external environment. A decrease in ROS production and an increase in SOD levels result in M2 polarization, which is accompanied by an increase in M2 markers and a decrease in M1 markers. To investigate the immunomodulatory effects

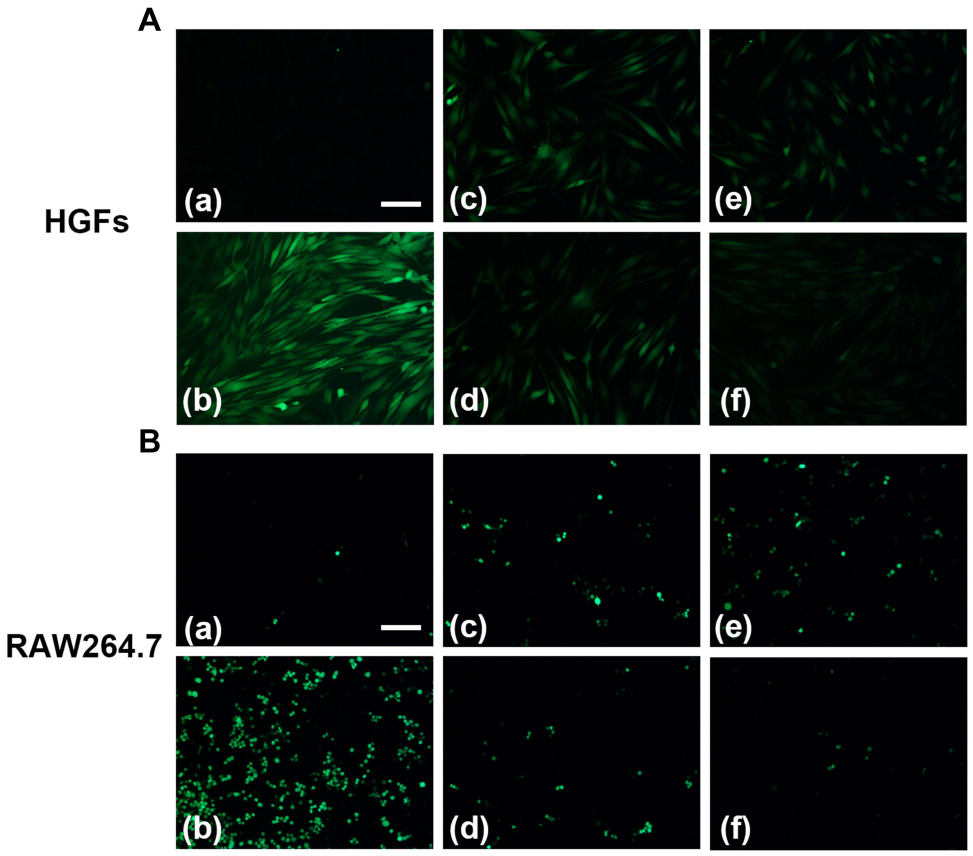

Figure 4 Scavenging efficiencies of NPs for ROS. Levels of ROS in HGFs (**A**) and RAW264.7 (**B**) cells were detected using a DCFH-DA fluorescent probe. (a) Control, (b) LPS, (c) HMPB, (d) HMPB@PDA, (e) Cur, (f) HMPB@Cur@PDA. Scale bar: 50 μm.

of the prepared NPs on the inflammatory response and polarization of macrophages, RAW264.7 cells were stimulated with LPS to mimic an inflammatory state, and macrophage phenotypes were detected by qPCR and ELISA. The presence of LPS significantly upregulated the mRNA expression levels of M1 markers TNF-α, IL-1β, and iNOS (Figure 5A–C). By contrast, although HMPB@PDA and Cur significantly downregulated inflammatory factors, HMPB@Cur@PDA showed stronger anti-inflammatory ability. Furthermore, compared with the LPS group, NPs containing HMPB promoted the expression of TGF-β, IL-10, and Arg-1 mRNA transcripts (Figure 5D–F).

To evaluate the effects of HMPB@Cur@PDA on macrophage polarization, macrophage phenotypes were determined by flow cytometry. CD80 and CD206 were used as markers of M1 and M2 macrophages, respectively. The flow cytometry results demonstrated that the proportion of cells expressing CD80 was lower in the HMPB@Cur@PDA-treated group, whereas the proportion of CD206-positive cells in HMPB@Cur@PDA group was significantly increased compared with the LPS-induced group (Figure S4A and B). The promotion of M2 marker expression by HMPB@Cur@PDA was enhanced by the synergistic effects of HMPB and Cur. These results indicated that RAW264.7 macrophages were polarized from the M1 to the M2 phenotype in the presence of HMPB@Cur@PDA. ELISA was used to further detect the levels of inflammatory factors in the culture supernatant (Figure 5G and H). Expression levels of TNF-α and IL-1β were significantly increased in the LPS group compared with the control group, and HMPB@Cur@PDA dramatically inhibited LPS-induced inflammatory factors. In addition, we investigated the effects of different NPs on the inflammation levels of periodontal cells including HGFs by qPCR (Figure 5I and J) and immunofluorescence (IF) (Figure 6). HGFs were incubated with LPS to establish an inflammation model. As expected, the expression levels of TNF-α and IL-1β genes were significantly decreased after HMPB@Cur@PDA treatment. The IF results for IL-1β showed that the levels of IL-1β protein in each treatment group were lower than those of the LPS group and similar to those of the control group.

Overall, the above results demonstrate that HMPB@Cur@PDA effectively scavenges ROS, downregulates the expression of inflammation-related factors, and modulates the phenotypic transition of macrophages from M1 to M2.

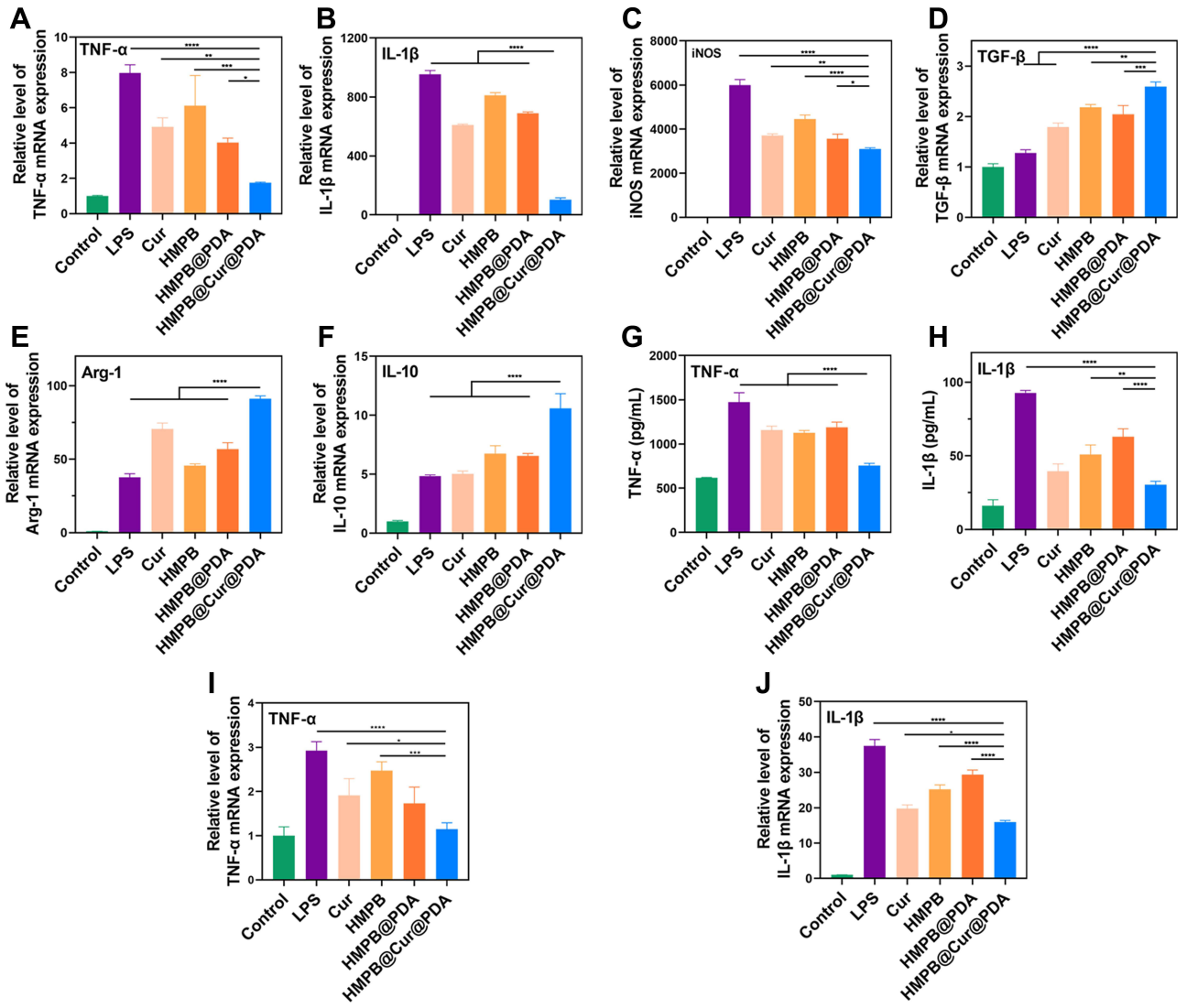

Figure 5 In vitro anti-inflammatory effects of HMPB@Cur@PDA via modulation of macrophage polarization. Gene expression of M1-related markers TNF-α (**A**), IL-1β (**B**), and iNOS (**C**), and M2-related markers TGF-β (**D**), Arg-1 (**E**), and IL-10 (**F**) after stimulation by LPS of RAW264.7 macrophages. Concentrations of pro-inflammatory factors TNF-α (**G**) and IL-1β (**H**) in RAW264.7 culture supernatant, mRNA levels of inflammation-related cytokines TNF-α (**I**) and IL-1β (**J**) in HGFs. n = 3, * $P < 0.05$, ** $P < 0.01$, *** $P < 0.001$, **** $P < 0.0001$.

HMPB@Cur@PDA Ameliorates Periodontal Disease

Having demonstrated the significant anti-inflammatory and antioxidant effects of HMPB@Cur@PDA NPs in vitro, we conducted an in vivo study to determine the efficacy of this nanocomposite in a periodontal disease model. Experimental periodontal disease was induced by local injection of LPS in a mouse model. Figure 7A illustrates the animal experimental procedure in detail. Mice facial photographs were recorded to visualize the treatment effects. As shown in Figure 7B, the gums and lips of the mice showed significant redness and swelling after LPS injection. A similar situation occurred in the Cur group, but the symptoms of gingival surface were slightly relieved compared with those observed in the LPS group. The incomplete elimination of LPS-induced inflammation by Cur may have been due to its low aqueous solubility and poor bioavailability. As expected, almost all of these local inflammatory reactions and redness disappeared after the administration of the HMPB@Cur@PDA nanocomplex. DCFH-DA was injected in situ, followed by in vivo fluorescence imaging to detect ROS levels at the infected site. The LPS inflammatory group exhibited the strongest and most extensive fluorescence signal, and the fluorescence decreased significantly after various treatments (Figure 8). We noted that the ROS levels in group HMPB were lower than those in group HMPB@PDA. It may be due to the PDA layer not being completely degraded to release the loaded HMPB. The insufficient concentration of HMPB nanozyme in the gingival tissue of group HMPB@PDA resulted in a higher level of ROS compared with group HMPB. No strong ROS

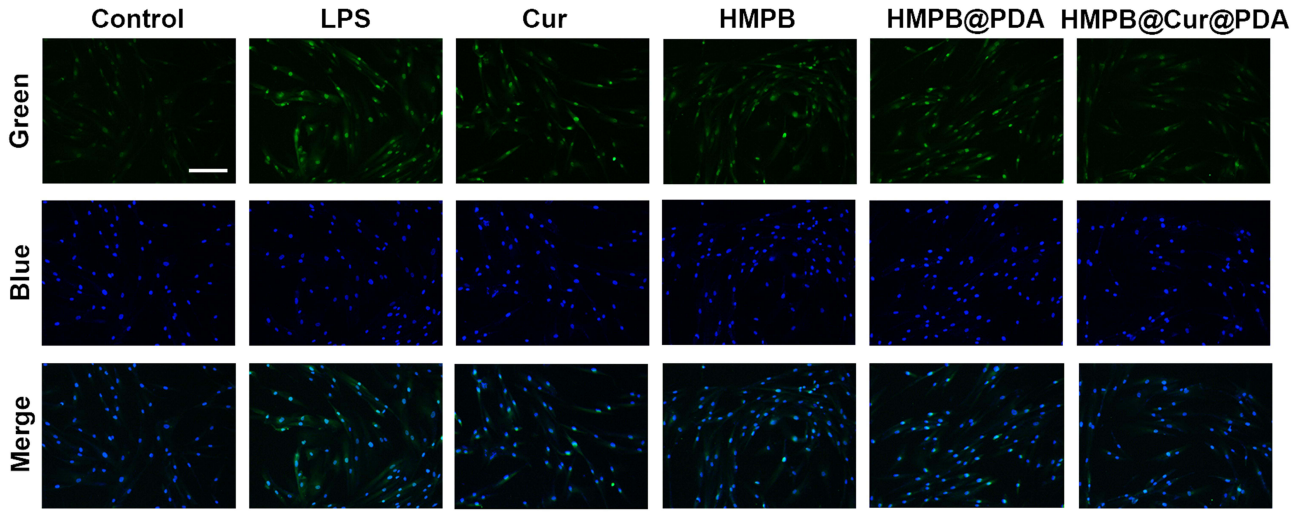

Figure 6 Representative IF staining of IL1β in HGFs treated with different NPs (scale bar: 50 μm).

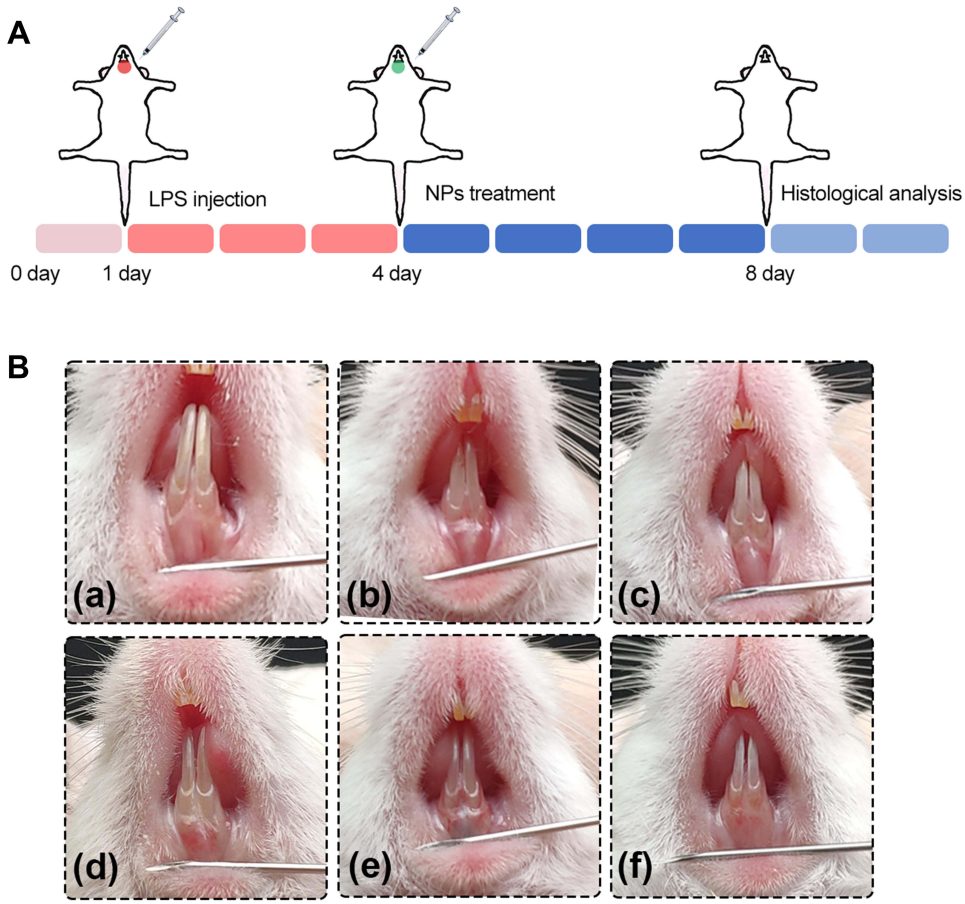

Figure 7 In vivo demonstration of anti-inflammatory capacity of different treatments in LPS-induced periodontal disease. (**A**) Schematic illustrations of whole in vivo experiments to evaluate the therapeutic efficacy of various NPs. (**B**) Intraoral images of mice after different treatments. (a) Control, (b) LPS, (c) Cur, (d) HMPB, (e) HMPB@PDA, and (f) HMPB@Cur@PDA.

fluorescence signal was detected in the HMPB@Cur@PDA group, similar to the blank control group. These results suggest that HMPB@Cur@PDA based on the PB nanozyme could alleviate local inflammation and effectively reduce local ROS levels in a mouse periodontal disease model.

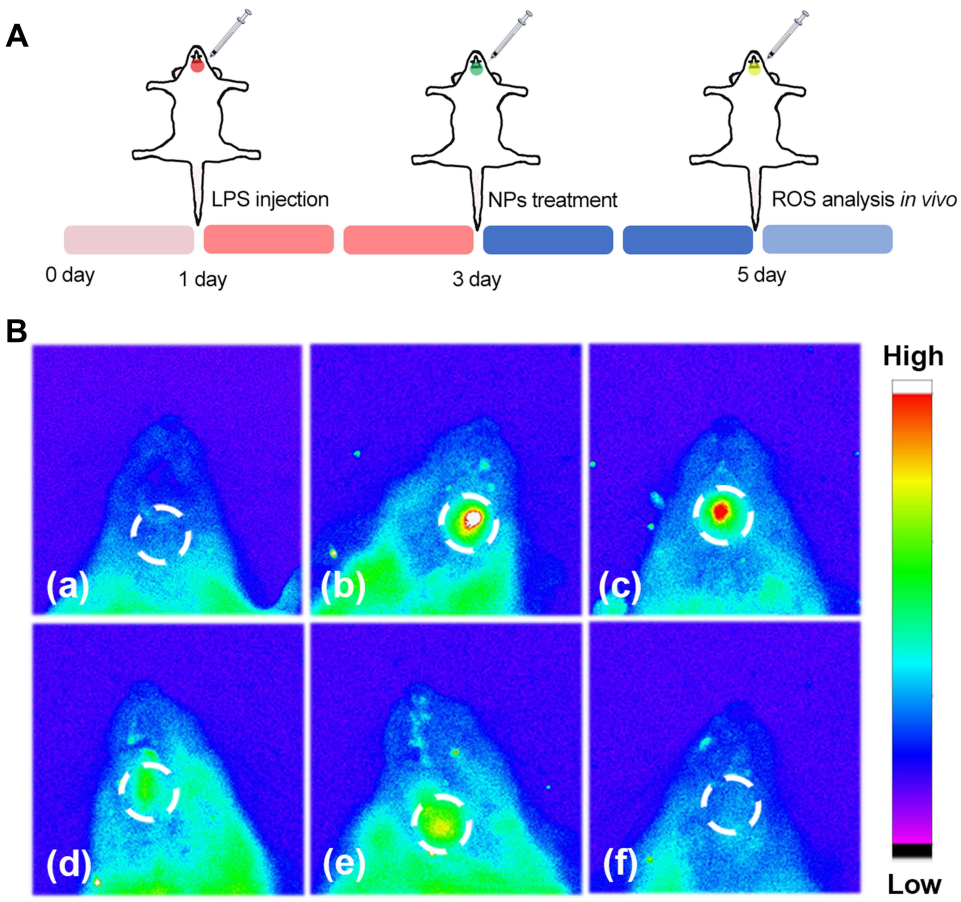

Figure 8 In vivo scavenging efficiencies of NPs for ROS. (**A**) Schematic illustrations of the evaluation of ROS in vivo. (**B**) Fluorescence images showing ROS levels in infected periodontal tissue with different treatments: (a) Control, (b) LPS, (c) Cur, (d) HMPB, (e) HMPB@PDA, and (f) HMPB@Cur@PDA.

The effects of different NPs on immune regulation were further investigated. H&E staining and IHC staining (Figure 9) were performed to characterize the histomorphology of the obtained periodontal tissue. H&E staining (Figure 9A) showed pathological changes in the gingival tissue region, with substantial infiltration of inflammatory cells and disorganized connective tissue structure in the periodontal tissues of the LPS inflammation model group, indicating an extensive inflammatory state. On the contrary, inflammatory cell infiltration was significantly reduced after treatment with different NPs and Cur, especially in the HMPB@Cur@PDA group. IHC staining of TNF-α and IL-1β (Figure 9B and C) showed similar results to the H&E staining. The relevant inflammatory factors were labeled with a brownish-yellow color. Compared with the control group, the LPS-induced inflammation group showed significant immunolabeling of TNF-α and IL-1β. In the treatment group, the expression of pro-inflammatory factors in the periodontal tissue of mice was significantly inhibited. In particular, the expression levels of TNF-α and IL-1β in the HMPB@Cur@PDA group decreased to the levels observed in the blank control group. These results were consistent with the RT-PCR results for the in vitro inflammation model. Taken together, the above findings indicate that HMPB@Cur@PDA nanocomposites inhibit inflammation and alleviate tissue destruction in periodontal disease.

Biocompatibility Evaluation

Biosafety is a major challenge for clinical applications of nanomaterials. We evaluated the effects of HMPB@Cur@PDA on blood routine parameters, physiological and biochemical markers in serum. As shown in Figure 10, there was no significant difference in blood routine parameters between the treatment group and the control group. In addition, typical liver function indicators (alanine aminotransferase (ALT) and aspartate aminotransferase (AST)) remained within normal

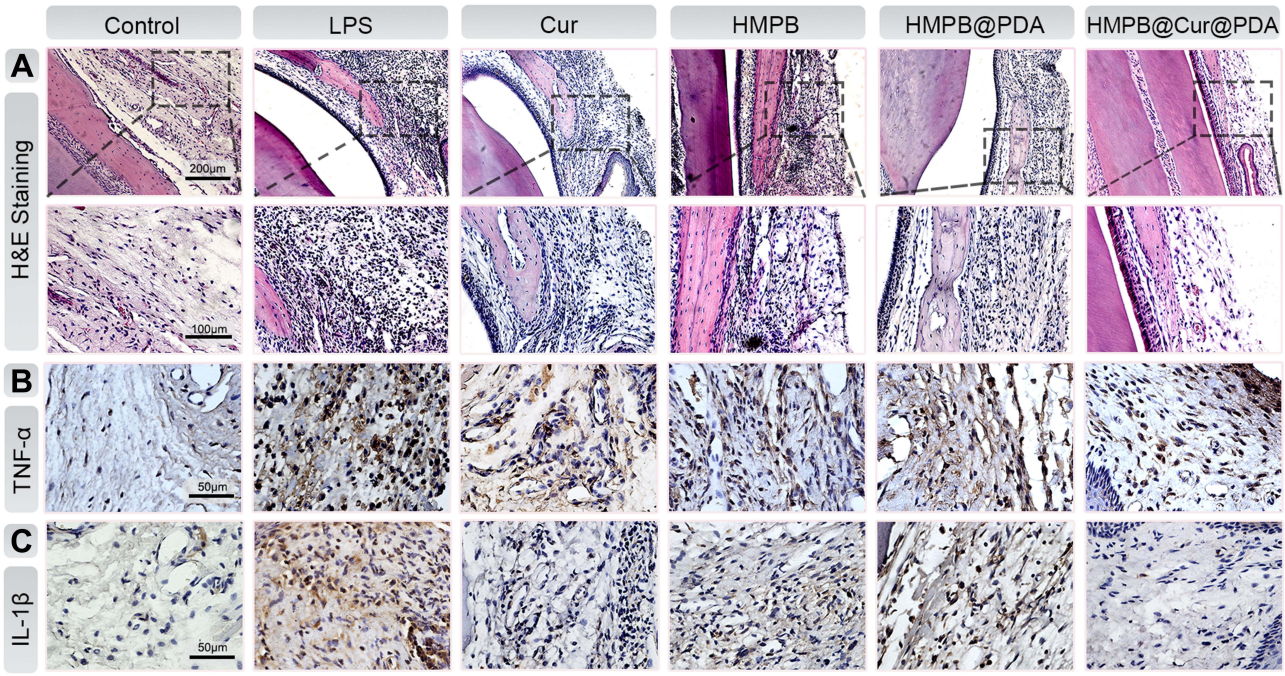

Figure 9 In vivo histological assessments of pathological features of periodontal inflammation after local injection of different nanomedicines. H&E staining (**A**) and IHC evaluation of (**B**) TNF-α and (**C**) IL-1β in periodontal tissues.

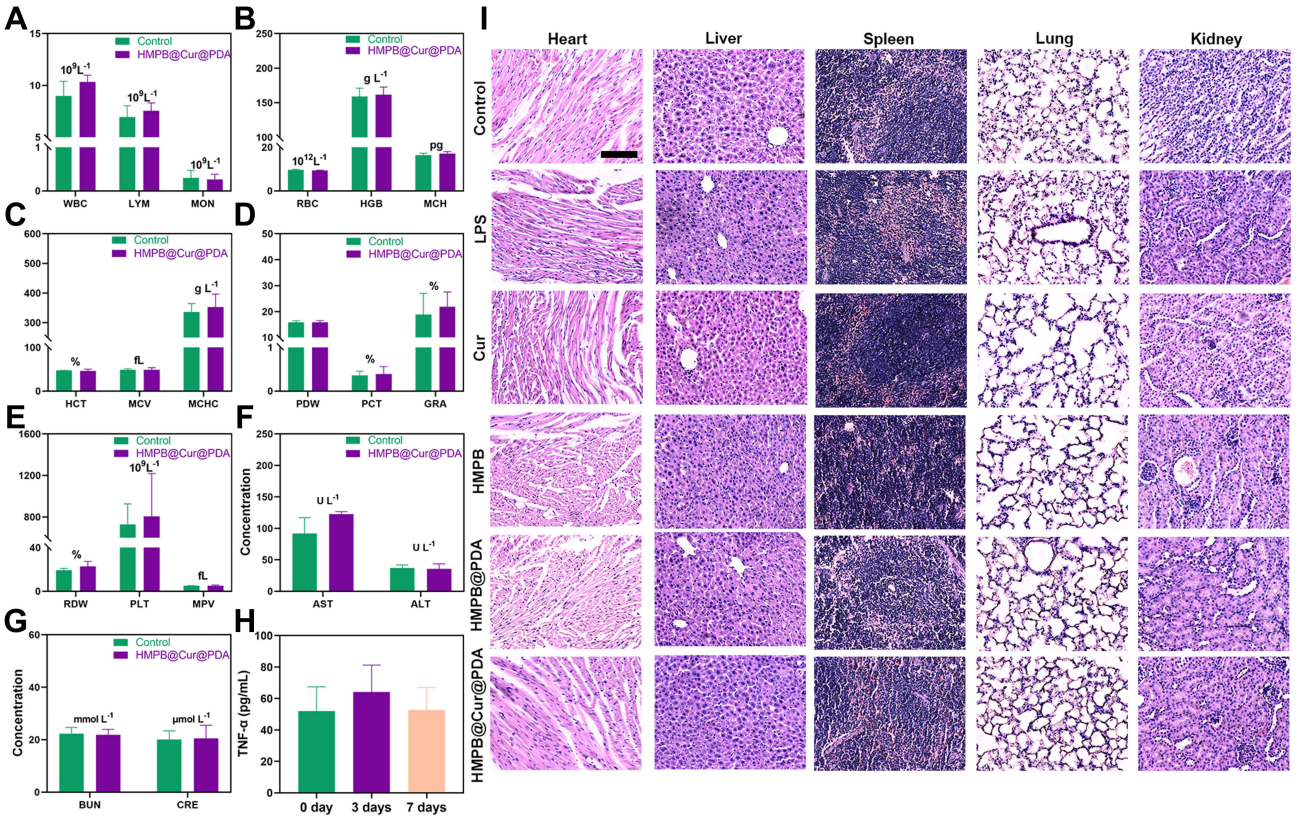

Figure 10 Biocompatibility assessment of HMPB@Cur@PDA. (**A–E**) Blood parameters of mice after local injection. (**F**) Serum levels of AST and ALT. (**G**) Serum levels of BUN and CRE. (**H**) TNF-α concentration in mouse serum after local injection of HMPB@Cur@PDA. (**I**) H&E staining of organs. Scale bar: 100 μm. Data are shown as mean ± SD (n = 3).

ranges, indicating no significant side effects on the liver. Renal function indicators including blood urea nitrogen (BUN) and creatinine (CRE) were similar to those of the control group, confirming that the NPs were not toxic to the kidneys. Histological changes were further assessed by H&E staining of major organs including heart, liver, spleen, lung, and kidney; no significant tissue inflammation was found in any organ. These results suggest that the as-prepared HMPB@Cur@PDA particles have a reasonably promising safety profile in vivo.

Conclusion

Overall, we designed and developed HMPB@Cur@PDA, a highly effective antioxidant defense platform based on the modulation of macrophage polarization. The relatively low pH and high levels of ROS in the inflammatory microenvironment compared with those in healthy tissues accelerate the release of HMPB and Cur by reacting with the PDA coating layer. This dual-response drug-triggered strategy improves the therapeutic efficacy of ROS scavengers. The results of in vitro experiments indicate that HMPB@Cur@PDA has excellent enzyme-like activity as well as free radical scavenging ability. In addition, HMPB@Cur@PDA can effectively scavenge intracellular ROS, reduce levels of pro-inflammatory factors such as TNF-α and IL-1β, and promote the secretion of anti-inflammatory factors including TGF-β and IL-10, thereby inducing polarization of macrophages from M1 to M2. In an oral and maxillofacial inflammatory disease model, HMPB@Cur@PDA effectively reduce the inflammatory reaction of periodontal tissues. Consequently, HMPB@Cur@PDA is a potential therapeutic strategy for periodontal tissue engineering and treatment of oral and maxillofacial inflammation or other inflammatory-like diseases.

Ethics Approval and Consent to Participate

Our study conformed to the Declaration of Helsinki. All animal procedures were performed in strict accordance with the Guidelines for the Care and Use of Laboratory Animals. The animal experimental procedures were approved by the Institutional Animal Care and Use Committee of Harbin Medical University (approved protocol no. SYDW2022-079), and the HGFs were isolated from the gingival tissue of orthodontic patients with approval by the Medical Ethics Committee of the Second Affiliated Hospital of Harbin Medical University (document no. KY2022-154). Before the study, informed consent was obtained from participants or from parents or guardians of participants under 18 years of age.

Funding

This work was supported by National Natural Science Foundation of China (Grant Nos. 81870736, 81801040, 81500816, 81570951) and the Natural Science Foundation of Heilongjiang Province of China (Grant No. YQ2020H018, LH2020H057).

Disclosure

The authors report no conflicts of interest in this work.

References

1. DeAngelis AF, Barrowman RA, Harrod R, Nastri AL. Maxillofacial emergencies: oral pain and odontogenic infections. *Em Med Australasia*. 2014;26(4):336–342. doi:10.1111/1742-6723.12266
2. Rastenienė R, Pūrienė A, Aleksejūnienė J, Pečiulienė V, Zaleckas L. Odontogenic maxillofacial infections: a ten-year retrospective analysis. *Surg Infect (Larchmt)*. 2015;16(3):305–312. doi:10.1089/sur.2013.264
3. Holmes CJ, Pellecchia R. Antimicrobial therapy in management of odontogenic infections in general dentistry. *Dental Clinics*. 2016;60(2):497–507. doi:10.1016/j.cden.2015.11.013
4. Kim MK, Chuang S-K, August M. Antibiotic resistance in severe orofacial infections. *J Oral Maxillofacial Surg*. 2017;75(5):962–968. doi:10.1016/j.joms.2016.10.039
5. Santosh ABR, Ogle OE, Williams D, Woodbine EF. Epidemiology of oral and maxillofacial infections. *Dental Clinics*. 2017;61(2):217–233. doi:10.1016/j.cden.2016.11.003
6. Suvan J, Petrie A, Moles DR, et al. Body mass index as a predictive factor of periodontal therapy outcomes. *J Dent Res*. 2014;93(1):49–54. doi:10.1177/0022034513511084
7. Hajishengallis G. Periodontitis: from microbial immune subversion to systemic inflammation. *Nat Rev Immunol*. 2015;15(1):30–44. doi:10.1038/nri3785
8. Ballance WC, Qin EC, Chung HJ, Gillette MU, Kong H. Reactive oxygen species-responsive drug delivery systems for the treatment of neurodegenerative diseases. *Biomaterials*. 2019;217:119292. doi:10.1016/j.biomaterials.2019.119292

9. Wang Y, Andrukhov O, Rausch-Fan X. Oxidative stress and antioxidant system in periodontitis. *Front Physiol*. 2017;8:910. doi:10.3389/fphys.2017.00910
10. Chapple IL, Matthews JB. The role of reactive oxygen and antioxidant species in periodontal tissue destruction. *Periodontol 2000*. 2007;43(1):160–232. doi:10.1111/j.1600-0757.2006.00178.x
11. Mahmoud AM, Desouky EM, Hozayen WG, et al. Mesoporous silica nanoparticles trigger liver and kidney injury and fibrosis via altering TLR4/NF-κB, JAK2/STAT3 and Nrf2/HO-1 signaling in rats. *Biomolecules*. 2019;9(10):528. doi:10.3390/biom9100528
12. Li Y, Guo F, Guan Y, et al. Novel anthraquinone compounds inhibit colon cancer cell proliferation via the reactive oxygen species/JNK pathway. *Molecules*. 2020;25(7):1672. doi:10.3390/molecules25071672
13. Zhou F, Mei J, Han X, et al. Kinsenoside attenuates osteoarthritis by repolarizing macrophages through inactivating NF-κB/MAPK signaling and protecting chondrocytes. *Acta Pharmaceutica Sinica B*. 2019;9(5):973–985. doi:10.1016/j.apsb.2019.01.015
14. Kalashnikova I, Chung S-J, Nafiujjaman M, et al. Ceria-based nanotheranostic agent for rheumatoid arthritis. *Theranostics*. 2020;10(26):11863–11880. doi:10.7150/thno.49069
15. Reinhold S, Blankesteijn WM, Foulquier S. The Interplay of WNT and PPARγ Signaling in Vascular Calcification. *Cells*. 2020;9(12):2658. doi:10.3390/cells9122658
16. Paul S, Chhatar S, Mishra A, Lal G. Natural killer T cell activation increases iNOS(+)CD206(-) M1 macrophage and controls the growth of solid tumor. *J Immunother Cancer*. 2019;7(1):208. doi:10.1186/s40425-019-0697-7
17. Tan H-Y, Wang N, Li S, Hong M, Wang X, Feng Y. The reactive oxygen species in macrophage polarization: reflecting its dual role in progression and treatment of human diseases. *Oxid Med Cell Longev*. 2016;2016:1–16. doi:10.1155/2016/2795090
18. Zhang L, Zhang L, Deng H, et al. In vivo activation of pH-responsive oxidase-like graphitic nanozymes for selective killing of Helicobacter pylori. *Nat Commun*. 2021;12(1):2002. doi:10.1038/s41467-021-22286-x
19. Ribeiro FM, de Oliveira MM, Singh S, et al. Ceria Nanoparticles Decrease UVA-Induced Fibroblast Death Through Cell Redox Regulation Leading to Cell Survival, Migration and Proliferation. *Front Bioeng Biotechnol*. 2020;8:577557. doi:10.3389/fbioe.2020.577557
20. Kim JW, Mahapatra C, Hong JY, et al. Functional Recovery of Contused Spinal Cord in Rat with the Injection of Optimal-Dosed Cerium Oxide Nanoparticles. *Adv Sci*. 2017;4(10):1700034. doi:10.1002/advs.201700034
21. Ibrahim HG, Attia N, Hashem FEZA, El Heneidy MAR. Cerium oxide nanoparticles: in pursuit of liver protection against doxorubicin-induced injury in rats. *Biomed Pharmacother*. 2018;103:773–781. doi:10.1016/j.biopha.2018.04.075
22. Yu Y, Zhao S, Gu D, et al. Cerium oxide nanozyme attenuates periodontal bone destruction by inhibiting ROS-NFκB pathway. *Nanoscale*. 2022;14(7):2628–2637. doi:10.1039/D1NR06043K
23. Berwin Singh S, Park H, Khang G, Lee D. Hydrogen peroxide-responsive engineered polyoxalate nanoparticles for enhanced wound healing. *Macromolecular Res*. 2018;26(1):40–47. doi:10.1007/s13233-018-6003-6
24. Zhang S, Ou Q, Xin P, Yuan Q, Wang Y, Wu J. Polydopamine/puerarin nanoparticle-incorporated hybrid hydrogels for enhanced wound healing. *Biomaterials sci*. 2019;7(10):4230–4236. doi:10.1039/C9BM00991D
25. Sahu A, Jeon J, Lee MS, Yang HS, Tae G. Antioxidant and anti-inflammatory activities of Prussian blue nanozyme promotes full-thickness skin wound healing. *Mater Sci Eng C Mater Biol Appl*. 2021;119:111596. doi:10.1016/j.msec.2020.111596
26. Zhang W, Hu S, Yin -J-J, et al. Prussian blue nanoparticles as multienzyme mimetics and reactive oxygen species scavengers. *J Am Chem Soc*. 2016;138(18):5860–5865. doi:10.1021/jacs.5b12070
27. Bai H, Kong F, Feng K, et al. Prussian Blue Nanozymes Prevent Anthracycline-Induced Liver Injury by Attenuating Oxidative Stress and Regulating Inflammation. *ACS Appl Mater Interfaces*. 2021;13(36):42382–42395. doi:10.1021/acsami.1c09838
28. Xie X, Zhao J, Gao W, et al. Prussian blue nanozyme-mediated nanoscavenger ameliorates acute pancreatitis via inhibiting TLRs/NF-κB signaling pathway. *Theranostics*. 2021;11(7):3213. doi:10.7150/thno.52010
29. Jing L, Shao S, Wang Y, Yang Y, Yue X, Dai Z. Hyaluronic Acid Modified Hollow Prussian Blue Nanoparticles Loading 10-hydroxycamptothecin for Targeting Thermochemotherapy of Cancer. *Theranostics*. 2016;6(1):40–53. doi:10.7150/thno.13250
30. Hu F, Zhou Z, Xu Q, et al. A novel pH-responsive quaternary ammonium chitosan-liposome nanoparticles for periodontal treatment. *Int J Biol Macromol*. 2019;129:1113–1119. doi:10.1016/j.ijbiomac.2018.09.057
31. Lin JH, Feng F, Yu MC, Wang CH, Chang PC. Modulation of periodontitis progression using pH-responsive nanosphere encapsulating metronidazole or N-phenacylthialzolium bromide. *J Periodontal Res*. 2018;53(1):22–28. doi:10.1111/jre.12481
32. Chang PC, Chao YC, Hsiao MH, et al. Inhibition of periodontitis induction using a stimuli-responsive hydrogel carrying naringin. *J Periodontol*. 2017;88(2):190–196. doi:10.1902/jop.2016.160189
33. Huang J, Wang Z, Krishna S, Hu Q, Xuan M, Xie H. Environment-sensitive hydrogels as potential drug delivery systems for the treatment of periodontitis. *Materials Express*. 2020;10(7):975–985. doi:10.1166/mex.2020.1705
34. Liu Y, Ai K, Lu L. Polydopamine and its derivative materials: synthesis and promising applications in energy, environmental, and biomedical fields. *Chem Rev*. 2014;114(9):5057–5115. doi:10.1021/cr400407a
35. Song Y, Zhu P, Xu Z, Chen J. Dual-Responsive Dual-Drug-Loaded Bioinspired Polydopamine Nanospheres as an Efficient Therapeutic Nanoplatform against Drug-Resistant Cancer Cells. *ACS Applied Bio Materials*. 2020;3(9):5730–5740. doi:10.1021/acsabm.0c00512
36. Zheng Q, Lin T, Wu H, et al. Mussel-inspired polydopamine coated mesoporous silica nanoparticles as pH-sensitive nanocarriers for controlled release. *Int J Pharm*. 2014;463(1):22–26. doi:10.1016/j.ijpharm.2013.12.045
37. Bai B, Gu C, Lu X, et al. Polydopamine functionalized mesoporous silica as ROS-sensitive drug delivery vehicles for periodontitis treatment by modulating macrophage polarization. *Nano Res*. 2021;14(12):4577–4583. doi:10.1007/s12274-021-3376-1
38. Forouzanfar F, Forouzanfar A, Sathyapalan T, Orafai HM, Sahebkar A. Curcumin for the management of periodontal diseases: a review. *Curr Pharm Des*. 2020;26(34):4277–4284. doi:10.2174/1381612826666200513112607
39. Zhou T, Chen D, Li Q, Sun X, Song Y, Wang C. Curcumin inhibits inflammatory response and bone loss during experimental periodontitis in rats. *Acta Odontol Scand*. 2013;71(2):349–356. doi:10.3109/00016357.2012.682092
40. Tan X, Kim G, Lee D, et al. A curcumin-loaded polymeric micelle as a carrier of a microRNA-21 antisense-oligonucleotide for enhanced anti-tumor effects in a glioblastoma animal model. *Biomaterials sci*. 2018;6(2):407–417. doi:10.1039/C7BM01088E
41. Zhao M-D, Li J-Q, Chen F-Y, et al. Co-delivery of curcumin and paclitaxel by "core-shell" targeting amphiphilic copolymer to reverse resistance in the treatment of ovarian cancer. *Int J Nanomedicine*. 2019;14:9453. doi:10.2147/IJN.S224579

42. Hu M, Furukawa S, Ohtani R, et al. Synthesis of Prussian blue nanoparticles with a hollow interior by controlled chemical etching. *Angewandte Chemie Int Edition*. 2012;51(4):984–988. doi:10.1002/anie.201105190
43. Song Y, Cai L, Tian Z, Wu Y, Chen J. Phytochemical curcumin-coformulated, silver-decorated melanin-like polydopamine/mesoporous silica composites with improved antibacterial and chemotherapeutic effects against drug-resistant cancer cells. *ACS omega*. 2020;5(25):15083–15094. doi:10.1021/acsomega.0c00912
44. Marie M, Bigot K, Angebault C, et al. Light action spectrum on oxidative stress and mitochondrial damage in A2E-loaded retinal pigment epithelium cells. *Cell Death Dis*. 2018;9(3):1–13. doi:10.1038/s41419-018-0331-5
45. Winterbourn CC. Reconciling the chemistry and biology of reactive oxygen species. *Nat Chem Biol*. 2008;4(5):278–286. doi:10.1038/nchembio.85
46. Ślesak I, Ślesak H, Zimak-Piekarczyk P, Rozpądek P. Enzymatic antioxidant systems in early anaerobes: theoretical considerations. *Astrobiology*. 2016;16(5):348–358. doi:10.1089/ast.2015.1328
47. Li -Y-Y, Cai Q, Li B-S, et al. The Effect of Porphyromonas Gingivalis Lipopolysaccharide on the Pyroptosis of Gingival Fibroblasts. *Inflammation*. 2021;44(3):846–858. doi:10.1007/s10753-020-01379-7
48. Yin S, Jia F, Ran L, et al. Exosomes derived from idiopathic gingival fibroma fibroblasts regulate gingival fibroblast proliferation and apoptosis. *Oral Dis*. 2021;27(7):1789–1795. doi:10.1111/odi.13707
49. Bao X, Zhao J, Sun J, Hu M, Yang X. Polydopamine nanoparticles as efficient scavengers for reactive oxygen species in periodontal disease. *ACS nano*. 2018;12(9):8882–8892. doi:10.1021/acsnano.8b04022
50. Albandar JM. Aggressive and acute periodontal diseases. *Periodontology*. 2014;65(1):7–12. doi:10.1111/prd.12013
51. Ni C, Zhou J, Kong N, et al. Gold nanoparticles modulate the crosstalk between macrophages and periodontal ligament cells for periodontitis treatment. *Biomaterials*. 2019;206:115–132. doi:10.1016/j.biomaterials.2019.03.039
52. Tian M, Chen G, Xu J, et al. Epigallocatechin gallate-based nanoparticles with reactive oxygen species scavenging property for effective chronic periodontitis treatment. *Chem Eng J*. 2022;433:132197. doi:10.1016/j.cej.2021.132197